Fabricating a Structured Single-Atom Catalyst via High-Resolution Photopolymerization 3D Printing

Jiachengjun Luo, Vincenzo Ruta, Ik Seon Kwon, Jody Albertazzi, Nicolò Allasia, Oleksii Nevskyi, Valentina Busini, Davide Moscatelli, and Gianvito Vilé*

This study introduces a novel solution to the design of structured catalysts, integrating single-piece 3D printing with single-atom catalysis. Structured catalysts are widely employed in industrial processes, as they provide optimal mass and heat transfer, leading to a more efficient use of catalytic materials. They are conventionally prepared using ceramic or metallic bodies, which are then washcoated and impregnated with catalytically active layers. However, this approach may lead to adhesion issues of the latter. By employing photopolymerization printing, a stable and active single-atom catalyst is directly shaped into a stand-alone, single-piece structured material. The battery of characterization methods employed in the present study confirms the uniform distribution of catalytically active species and the structural integrity of the material. Computational fluid dynamics simulations are applied to demonstrate enhanced momentum transfer and light distribution within the structured body. The materials are finally evaluated in the continuous-flow photocatalytic oxidation of benzyl alcohol to benzaldehyde, a relevant reaction to prepare biomass-derived building blocks. The innovative approach reported herein to manufacture a structured single-atom catalyst circumvents the complexities of traditional synthetic methods, offering scalability and efficiency improvements, and highlights the transformative role of 3D printing in catalysis engineering to revolutionize catalysts' design.

1. Introduction

Catalysts play a central role in chemistry as they can alter the course of a reaction, making the production of target chemicals more streamlined.[1] In particular, homogeneous catalysts prove highly efficient as they offer an extensive surface area exposed to the reactants and precise ligand engineering affecting the steric and electronic properties of the active metal centers. However, disadvantages in their employment include difficulties in catalyst separation from reaction mixtures, which makes their recycling and reuse in further processes less appealing, significantly limiting their usage in many industrial applications. To overcome such limitation, significant efforts have been dedicated to the development of heterogeneous catalysts.[2–4] In this context, single-atom catalysts represent the ultimate frontier in catalysis, as they maximize atom utilization, exhibit tunable coordination environments around the individually dispersed active species, and possess unique physicochemical and electronic properties that positively impact their reactivity and selectivity in many processes of interest, including CO_2 reduction reactions, cyclizations and selective hydrogenations.[5,6] Over the past years, considerable endeavors have been allocated to broaden single-atom catalysts application across a range of fields, spanning from thermal catalysis[7–11] to photocatalysis[12–15] and electrocatalysis.[16,17] These materials can be prepared through a wide set of synthesis strategies which include impregnation,[18] copolymerization,[19] photocatalytic reduction,[20] freeze deposition,[21] atomic layer deposition,[22] and pyrolysis of metal-organic frameworks.[23] Even if widely employed in small scale laboratory setups, powdered catalysts show limitations that hinder their application on a large scale. For example, handling and separating fine powders from reaction mixtures presents inherent challenges.[24] Moreover, catalysts agglomeration may occur during the process, resulting in a decrease of their surface area available to interact with the reaction mixture, and subsequently impacting their overall catalytic efficiency.[25] To confront these challenges effectively, a transition from conventional methods of preparing catalytic materials in powdered form toward the adoption of strategies aimed at the synthesis of structured catalysts emerges as essential.

J. Luo, V. Ruta, J. Albertazzi, N. Allasia, V. Busini, D. Moscatelli, G. Vilé
Department of Chemistry, Materials and Chemical Engineering "Giulio Natta"
Politecnico di Milano
Piazza Leonardo da Vinci 32, Milano 20133, Italy
E-mail: gianvito.vile@polimi.it

I. S. Kwon
Pohang Accelerator Laboratory
Pohang University of Science and Technology
80 Jigok-ro 127beongil, Pohang 37673, Republic of Korea

O. Nevskyi
Third Institute of Physics – Biophysics
Georg-August University
Friedrich-Hund-Platz 1, 37077 Göttingen, Germany

**ADVANCED
SCIENCE NEWS**

www.advancedsciencenews.com

**ADVANCED
FUNCTIONAL
MATERIALS**

www.afm-journal.de

Structured catalysts are often prepared via meticulously orchestrated synthetic procedures, where the catalytically active material is deposited on a structured support, such as a honeycomb monolith,[26,27] metallic foam,[28] or a porous ceramic substrate.[29] This approach involves a washcoating step of the structured support followed by the impregnation of the resulting structure with a metal salt solution to ensure an even distribution of active species across the whole catalyst body. Structured supports are traditionally produced via extrusion or molding;[30,31] nonetheless, complex architectures that are not achievable employing such manufacturing processes can be fabricated resorting to 3D printing.[32,33] This approach offers an innovative design space for structured catalysts, allowing for the accurate tuning of the size and length of flow channels, and the precise control over the catalytic layer thickness and mechanical properties. In this context, our group recently reported the fabrication of a structured reactor featuring a 3D-printed metal-based support coated with a single-atom catalytic layer.[34] Similarly, Vilar et al. published the coating of the surface of a Kenics commercial static mixer with photocatalytic materials (i.e., TiO_2, Fe_2O_3) and applied the system to the photocatalytic degradation of pollutants in continuous-flow mode.[35] Despite the novelty, challenges in the application of 3D printing approaches in catalysis persist, including the need to achieve an optimal dispersion of the catalyst layer on the support material and the potential risk of detachment of such layer from the support itself, resulting in lower stability and efficiency of the catalytic system. Overcoming these challenges is essential for accomplishing the full potential of structured technical catalysts, especially in view of their scalability and cost-effectiveness application in industrial scenarios.[36,37]

To avoid adhesion issues in structured catalysts, an optimal preparation strategy should involve the fabrication of their components or bodies exploiting 3D printing techniques. This holistic approach offers several potential solutions to bypass adhesion challenges and enhances the performance and reliability of the produced parts in catalysis engineering settings.[38] Single-piece additive manufacturing, through which the entire catalytic body is printed as a cohesive unit, does not require the assembly of multiple parts together after the corresponding printing process, thus minimizing potential adhesion issues between the individual components and the need for additional post-processing steps.[39] Moreover, the employment of advanced printing technologies, such as continuous liquid interface production (CLIP) or multi-material printing, allows for an enhanced control over the printing process itself while simultaneously improving adhesion between layers.[40] A commonly employed method for CLIP is photopolymerization, which takes advantage of ultraviolet wavelengths to selectively solidify liquid resin, leading to the fabrication of a 3D structure as a stand-alone and single-piece body.[41,42] Moreover, photopolymerization techniques based on digital light processing enable a higher precision and degree of detailing of the structured catalyst architectures, which in turn allows for the production of complex geometries with fine features,[43] superior surface resolution,[44] and faster printing speeds that contribute to efficient and time-effective production processes.[45] This plethora of advantages makes photopolymerization a widely applied printing technology for applications where precision, surface details, and material versatility are combined with the need for a single-piece technical body.

In this study, we present an innovative strategy for the preparation of a stand-alone, single-piece single-atom catalyst body consisting in the direct shaping of single-atom catalyst powders via photopolymerization without any intermediate washcoating step. We based the architecture of the structured catalytic bodies on the Kenics static and dynamic mixers, renowned for their helical twist bowtie design and "split-and-recombine" feature. To the best of our knowledge, this is the first time a photopolymerization route is applied to produce a catalytic body comprising a single-atom catalyst supported on carbon nitride. The stability and reactivity of the as-synthesized materials were tested in a relevant continuous-flow photocatalytic application, namely the benzyl alcohol oxidation. We believe that this work holds the potential to revolutionize the field of structured catalyst design by providing a more controlled and efficient means of fabricating catalytically active structures with enhanced properties in several industrial applications.

2. Results and Discussion

2.1. Synthesis and Characterization of Powdered Catalysts

A nickel-containing single-atom catalyst (SAC) was synthesized with a hard template-assisted copolymerization route reported elsewhere. Briefly, cyanamide was added to an aqueous solution of nickel chloride ($NiCl_2$), serving as a Ni source for the isolated active metal species, and an aqueous suspension of SiO_2, acting as the hard template for the formation of mesopores in the carbon nitride (CN_x) support. Upon water evaporation, the obtained solid was calcined at 550 °C to allow for the polymerization of cyanamide and the immobilization of the Ni single atoms on the CN_x itself. The SiO_2 template was then removed treating the yellow solid with an aqueous solution of ammonium bifluoride (NH_4HF_2) for 24 h. At the end of the synthesis procedure, a $Ni_1@mpgCN_x$ SAC was obtained as well as, for comparison purposes, the bare $mpgCN_x$ support material (**Figure 1a**). The subscript "1" after the metal highlights the single-atomic nature of the active centers within the catalysts, and the "mpg" acronym refers to the mesoporous graphitic nature of the CN_x support.

Before stability and photocatalytic experiments, the textural and physicochemical properties of the powdered materials were investigated through a battery of bulk and surface characterization techniques. The elemental analysis showed that both $Ni_1@mpgCN_x$ and $mpgCN_x$ have a C/N ratio in the 0.60–0.70 range, in agreement with data reported in the literature for this class of materials, and close to the theoretical nominal value of 0.75 for the CN_x structure.[46] The slight deviation of the experimental C/N values toward the lower end of the 0.60–0.70 interval was attributed to the presence of small amounts of impurities, notably oxygen and hydrogen, which are commonly encountered in such materials owing to incomplete polymerization of the precursors and their exposure to air.[47] The loading of nickel in $Ni_1@mpgCN_x$ was confirmed by inductively coupled plasma optical emission spectroscopy (ICP-OES) analysis, which yielded a corresponding metal content of 1.6 wt% in the catalyst. Elemental analysis and ICP-OES data for the powdered
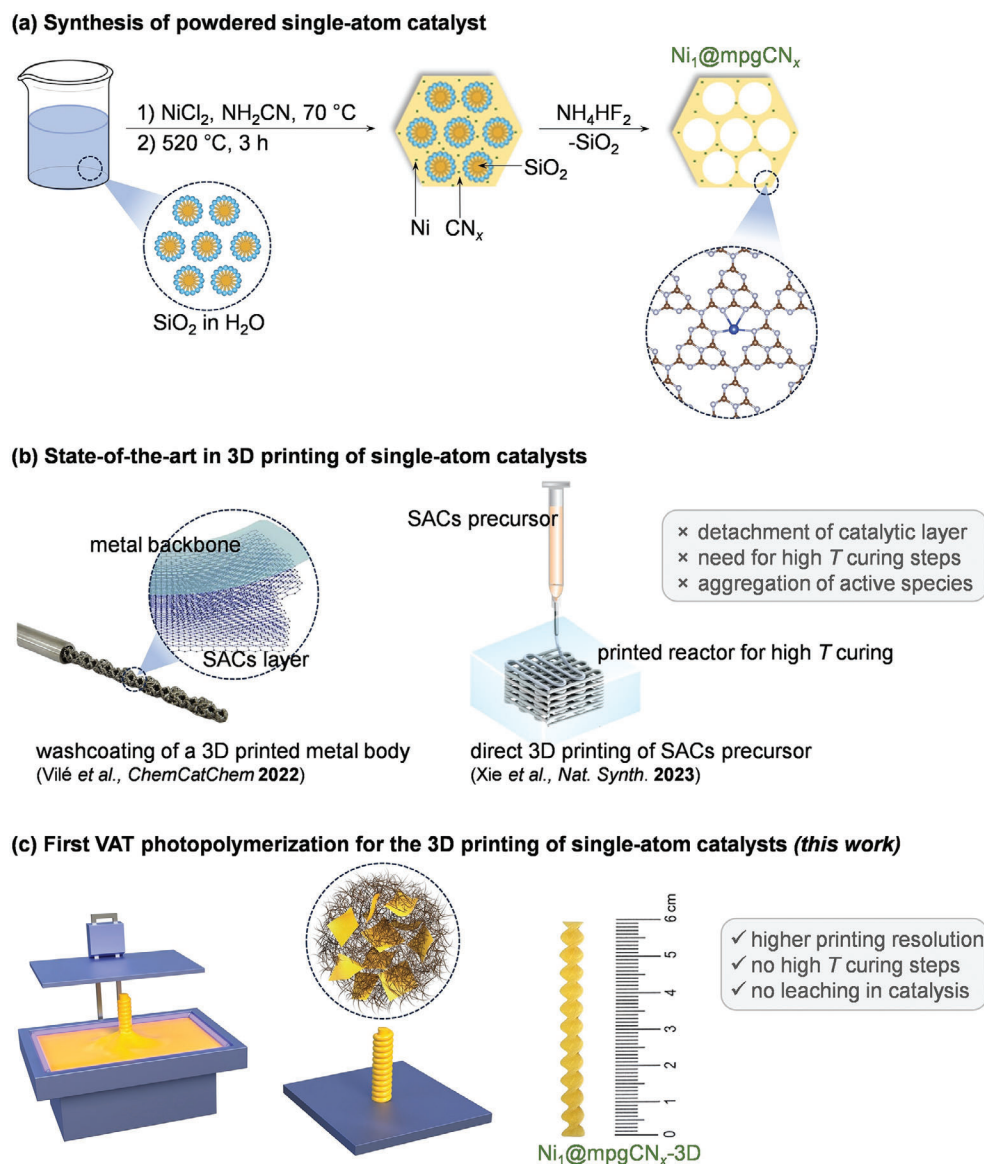
Figure 1. Hard template-assisted copolymerization strategy applied for the synthesis of the powdered catalysts a); state-of-the art of SACs 3D printing techniques b); novel approach for SACs 3D printing via VAT photopolymerization: this method is based on continuous digital light processing, which rapidly and continuously cure the resin exploiting a projected, dynamically-controlled light source, enabling faster printing speeds and consistent layer formation c).

catalyst are reported in **Table 1**. To assess the monoatomic distribution of the metal sites in $Ni_1@mpgCN_x$, transmission electron microscopy combined with energy-dispersive X-ray spectroscopy (TEM-EDX) was employed. Figure S5 (Supporting Information) displays the absence of major metal clusters, thus confirming the individual dispersion of the Ni active centers on the CN_x support. Fourier-transform infrared spectroscopy (FTIR) measurements were carried out to elucidate the bond system of the catalysts (**Figure 2a**). Infrared spectra of the samples present a broad band in the 3400–3100 cm^{-1} region ascribed to stretching vibrational modes of uncondensed primary (–NH–) and secondary (–NH_2) amines present in the CN_x architecture, reflecting the incomplete polymerization in the support.[48] A series of sharper peaks lo-

cated at lower wavenumber values, between 1700 and 1100 cm^{-1}, were assigned to C–N and C = N stretching vibrations of the aromatic repeating units that compose the core structure of CN_x.[49] Notably, the FTIR spectra of $Ni_1@mpgCN_x$ and bare $mpgCN_x$ present only minor differences, demonstrating that the introduction of metal atoms into the $mpgCN_x$ framework does not cause significant chemical disruption or rearrangement of the support architecture. Sample crystallinity was evaluated through X-ray diffraction (XRD) measurements. In the diffractograms of the powdered catalysts (Figure 2d), the peaks centered at $2\theta = 13°$ and at 27° were attributed to the (100) and (002) planes of the carbon nitride system, respectively.[50] The absence of additional diffraction features in the diffractograms, possibly correlated to

Table 1. Elemental composition and surface area of the powdered and structured catalysts.

Catalyst	C[a] (wt%)	N[a] (wt%)	H[a] (wt%)	C/N (-)	Ni[b] (wt%)	S_{BET}[c] (m^2 g^{-1})
mpgCN$_x$	21.07	31.98	2.59	0.66	-	187
Ni$_1$@mpgCN$_x$	20.52	31.21	2.35	0.66	1.6	166
mpgCN$_x$-3D	56.99	3.54	8.88	0.16	-	7
Ni$_1$@mpgCN$_x$-3D	57.13	3.71	8.35	0.15	0.016	7

[a] C, N, and H content from combustion analysis; [b] ICP-OES data; [c] BET method applied on the adsorption branch of the N$_2$ isotherm in the 0.05 < p/p_0 < 0.3 range.

the presence of Ni clusters or nanoparticles, further confirms the single-atom nature of the active centers in Ni$_1$@mpgCN$_x$. Additional insights into the molecular architecture of Ni$_1$@mpgCN$_x$ and mpgCN$_x$ were assessed by cross-polarization/magic angle spinning (CP/MAS) ^{13}C NMR spectroscopy (Figure 2b). The two peaks observed in the NMR spectra of both CN$_x$-based catalysts, localized at 156.3 and 164.6 ppm, were assigned to the presence of carbon atoms interacting with three aromatic nitrogen atoms, and to carbons simultaneously bonded to two aromatic nitrogens and a defective amine site, respectively, confirming once again the CN$_x$ architecture of the freshly produced powdered catalysts.[51]

2.2. Photopolymerization-Driven Shaping of Structured Catalysts and Characterization

Ni$_1$@mpgCN$_x$ and mpgCN$_x$ were shaped into structured bodies via VAT photopolymerization additive manufacturing, through

which a liquid photopolymeric resin was first mixed with each powdered photocatalyst, and the resulting suspensions were then used as "ink" to print the catalytic bodies layer by layer. Despite the significant advantages of single-atom catalyst manufacturing via 3D printing, only few examples have been reported in the literature, depicted in Figure 1b. In our previous work, we designed a structured reactor consisting in a metal-based support produced via 3D printing, which was then coated with a single-atom catalytic layer, showing noteworthy performance in the continuous-flow hydrogenation of biomass-derived aldehydes.[34] Another printing technique that has already been reported in the literature involves a gelatin-based 3D inkjet printing method.[52] The novel 3D printing fabrication process described in this study offers unique advantages over the previously mentioned catalyst structuring methods. The primary advantage of employing a full-body 3D-printed catalytic structure is reducing the likelihood of detachment of the catalytic layer, a common issue when dealing with supports produced via 3D printing and subsequently coated with a catalytic layer. Additionally, the synthetic method
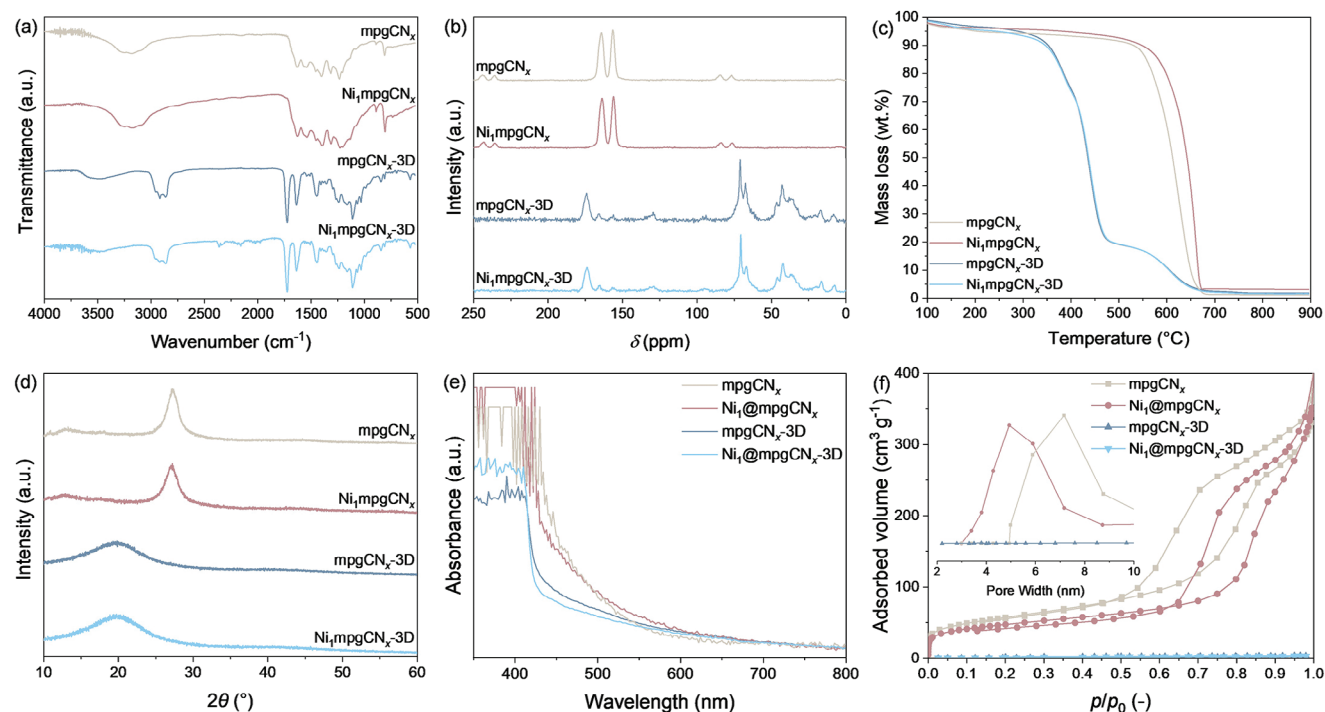

Figure 2. FTIR spectra a), CP/MAS ^{13}C NMR spectra b), TGA curves c), XRD patterns d), UV–vis absorption spectra e), and N$_2$ adsorption/desorption isotherms f) of mpgCN$_x$, Ni$_1$@mpgCN$_x$, mpgCN$_x$-3D and Ni$_1$@mpgCN$_x$-3D. Inset in f) shows qualitative data of pore diameter distribution within the catalysts.

**ADVANCED
SCIENCE NEWS**

www.advancedsciencenews.com

**ADVANCED
FUNCTIONAL
MATERIALS**

www.afm-journal.de

outlined in the present study is more straightforward compared to the washcoating procedures exploited in previous works, and it eliminates the need for high-temperature curing steps required in other 3D-printing techniques (e.g., the gelatin-based inkjet printing method) that could lead to metal aggregation and disruption of the single-atom architectures. Moreover, to the best of our knowledge, this is the first reported example of VAT photopolymerization applied to the fabrication of single-atom catalysts, enabling also superior resolution in the shaping of catalytic bodies.

Ultraviolet (UV) irradiation was employed to initiate the curing or polymerization process of the resin at targeted locations, and a mechanized platform facilitated the incremental downward movement of the object being fabricated after the completion of each layer of the catalytic bodies. Since the preparation process involved the use of liquid media, no mechanical or structural support was required during the fabrication step. More specifically, the powdered $Ni_1@mpgCN_x$ and $mpgCN_x$ were mixed with the polymeric resin – the latter selected with suitable rheological properties for printing and shape retention –, and the resulting mixture was sonicated to ensure a homogeneous dispersion of the CN_x-based materials in the final 3D-printed structured catalysts. The mixture was then loaded onto the printer vat, and subsequently exposed to UV light irradiation that allowed for the body fabrication in a layer-by-layer manner. The synthesis strategy employed for the preparation of the two powdered catalysts ($Ni_1@mpgCN_x$ and $mpgCN_x$), and the 3D printing process applied for the fabrication of the two corresponding catalytic bodies (from here on, referred to as $Ni_1@mpgCN_x$-3D and $mpgCN_x$-3D) are illustrated in Figure 1c. A series of catalyst-to-resin mass ratio have been tested, ranging from higher to lower than 1:100. As a result, employing higher quantities of powdered precursors (e.g., 1:80, 1:50) led to clogging of the 3D printer channels during the printing process, compromising the structural stability and integrity of the produced catalysts. Conversely, higher dilutions of the powdered catalysts (e.g., 1:200, 1:300) posed no structural issues; however, the extremely low content of metal species resulted in a reduced reaction performance of the reactor systems. For these empirical reasons, we decided to produce 3D-printed catalytic bodies with a catalyst-to-resin mass ratio of 1:100.

As a model to shape the architecture of the 3D-printed bodies, we took inspiration from the Kenics static and dynamic mixers. In these structures, the helical twist bowtie, along with their "split-and-recombine" feature, makes such architecture highly suitable for continuous-flow experiments, particularly with low-Reynolds number fluids. Thus, we intentionally selected a geometry evocative of spiral-shaped twists rather than a conventional cylindrical structure, aiming at exploiting the advantageous features inherent to that specific configuration, including an enhanced surface-to-volume ratio. This is regarded as a critical aspect when dealing with reactions predominantly occurring at the interface between two media, and higher values of such ratio ultimately lead to a higher efficiency of the catalytic system.[53] Furthermore, the spiral-shaped geometry promotes increased turbulence motions of the reaction solution within the reactor, thus favoring improved mass and heat transfer processes along the catalytic process thanks to an enhanced mixing of reactants and products.[54] In addition, such body geometry favors an improved irradiation of the reactive solution, positively impacting photo-

catalytic reactions where light plays a crucial role in driving the catalytic process.[55] By leveraging these inherent advantages of a spiral-shaped architecture, our aim was to enhance the overall catalytic performance of the 3D-printed reactors in photocatalytic processes. While designing the structured catalysts, an additional challenge arose from the possible presence of nickel atoms deeply buried within the 3D-printed structure and, as a consequence, not available during the catalytic processes. To address this issue, we opted for a 3D-printed architecture with minimal thickness, aiming at maintaining its mechanical stability while maximizing the exposure of the greatest number of active metal species to the reaction.

Elemental analysis of the reactor structured body prepared via additive manufacturing confirmed the effective presence of the powdered catalysts ($Ni_1@mpgCN_x$-3D and $mpgCN_x$) in the corresponding $Ni_1@mpgCN_x$-3D and $mpgCN_x$-3D structures, with a substantial increase in the carbon contents due to the carbonaceous composition of the resin itself. The content of metal active species in the Ni-containing 3D-printed body (0.016 wt%) was in line with the dilution factor of the powdered SAC with the resin (1:100).

The surface area and porosity of the materials were evaluated through N_2 physisorption measurements (Figure 2f), and the obtained values underscored the non-porous, bulk nature of the prepared reactor bodies. The presence of Ni atoms in the CN_x framework did not to affect the printing process and the surface area of $Ni_1@mpgCN_x$-3D.

The main signals observed in the infrared spectra of the 3D-printed catalysts were assigned to vibrational modes proper of the resin bond system which includes polycarbonate and polyvinyl alcohol moieties. The broad band enclosed in the 3700–3400 cm^{-1} region contains contributions ascribed to O–H stretching vibrations related to the presence of alcoholic groups within the resin structure. An additional broad signal in the 3000–2800 cm^{-1} wavenumber range was detected, arising from a plethora of C–H stretching modes characteristic of the aliphatic chains in the resin.[56] The peak at 1725 cm^{-1} was assigned to the C = O stretching vibrations of carbonyl functional groups, while contributions below this frequency were mainly attributed to vibrational modes connected to the aliphatic backbone of the resin structure.[57] Notably, also in this case, the infrared spectrum of the structured catalyst containing Ni species ($Ni_1@mpgCN_x$-3D) presented no evident differences from that of the body fabricated using only bare $mpgCN_x$ ($mpgCN_x$-3D).

XRD spectra of $Ni_1@mpgCN_x$-3D and $mpgCN_x$-3D displays a broad diffraction feature centered at $2\theta = 20°$, indicating the overall amorphous nature of the tridimensional architecture of these catalysts. Furthermore, the disappearance of the two typical CN_x-related peaks at $2\theta = 13°$ and $27°$ may be explained by the 1:100 dilution of the powdered catalysts within the resin. Thermogravimetric analyses (TGA) were conducted on the powdered catalysts and 3D-printed structured materials to evaluate their thermal stability (Figure 2c). The resulting curves of both $Ni_1@mpgCN_x$-3D and $mpgCN_x$-3D show a first mass loss occurring at ≈100 °C, caused by the desorption of water molecules from the structured bodies, and two additional weight drops in the 380–430 °C range (corresponding to a mass loss of ≈80%) and at ≈565 °C, featuring the complete degradation of the materials. While the second mass loss was mainly attributed to the degradation of the resin,
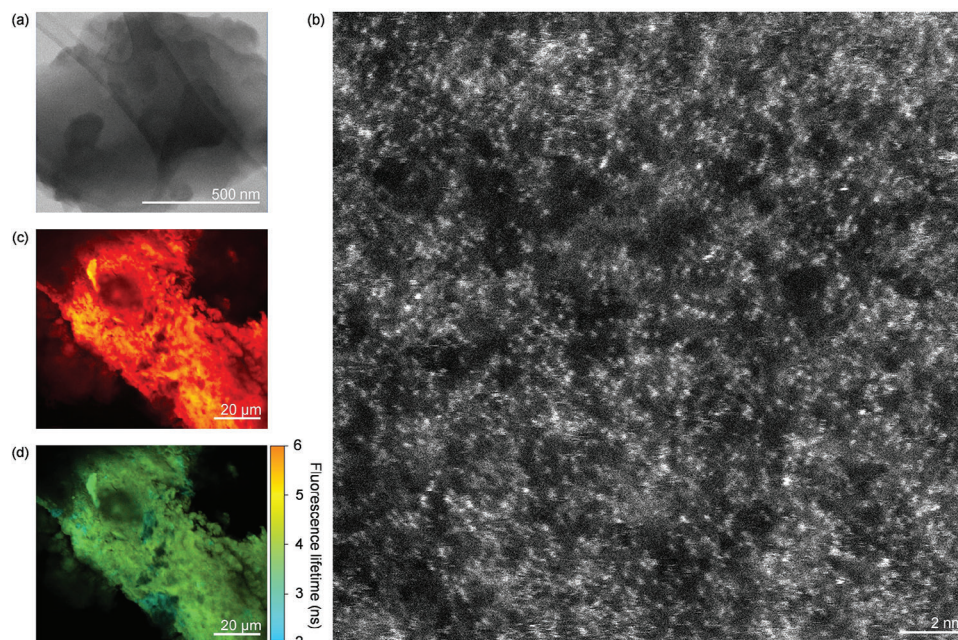
Figure 3. TEM micrograph a), HAADF-STEM image b), CLSM micrograph c), and FLIM image d) of the Ni$_1$@mpgCN$_x$-3D structured catalyst.

the third was ascribed to the decomposition of CN$_x$, as demonstrated by the presence of the latter in the TGA profiles of both Ni$_1$@mpgCN$_x$ and mpgCN$_x$. UV–vis spectra (Figure 2e) show a wide absorption band at wavelengths greater than 400 nm, in accordance with data reported in the literature regarding CN$_x$-based materials.[58] Characterization measurements related to the 3D-printed resin alone, not loaded with any powdered catalysts, are reported in Figure S6 (Supporting Information)

TEM micrographs were acquired (**Figure 3a**) to evaluate the morphological and topological features of the structured bodies. The images elucidated the regular architecture of the 3D-printed catalysts, as well as the absence of major metal clusters deriving from nickel aggregation. The distribution of the Ni active species was further assessed by high-angle annular dark-field scansion transmission electron microscopy (HAADF-STEM). Ni atoms representing the catalytically-active centers were clearly identified as individually isolated bright spots (Figure 3b), thus confirming the monoatomic and homogeneous dispersion of the powdered catalysts during the printing process and, once again, the absence of metal clusters or nanoparticles. To investigate the internal structure of the 3D-printed catalysts, we turned to confocal laser scanning microscopy (CLSM): the catalytic bodies were cut and labeled with the Nile Red dye (for detailed labeling procedure, see the Experimental Section), which is commonly employed for visualizing polymers[59,60] and material structures.[61] This dye exhibits minimal fluorescence in water or other polar environments, but the emission of photons increases upon its non-covalent interaction with apolar structures, such as the photopolymer used as resin. The Nile Red dye allowed for the observation of the extremely uniform structure in the 3D-printed materials (Figure 3c), with a consistent distribution of organic/inorganic components and precise internal configuration, reflecting careful manufacturing in the fabrication process. Through fluorescence-lifetime imaging microscopy (FLIM), an

image can be produced based on the differences in the excited state decay rate from a fluorescent sample. This offers a way to intensify imaging since fluorescence lifetime is unaffected by the fluorophore concentration and the specific spectral sensitivity of the detection system.[62] Therefore, we performed FLIM on the Ni$_1$@mpgCN$_x$-3D sample, confirming both the homogeneity in its overall structure and in the incorporation of CN$_x$ within the resin matrix, as these former regions exhibit shorter lifetimes, as depicted in Figure 3d. Tridimensional cross section of the Ni$_1$@mpgCN$_x$-3D structured material was elucidated via microtomographic analysis, further confirming a homogeneous and smooth structure of the material in its cross section, as well as the absence of any major irregularities deriving from the 3D printing process. The complete reconstruction of the 3D-printed bodies was derived from the individual cross-section tomographic micrographs (Figure S7, Supporting Information) and is available in Video S1 (Supporting Information).

X-ray absorption spectroscopy (XAS) measurements at the Ni K-edge were performed to elucidate the electronic and local structure around the nickel atoms in Ni$_1$@mpgCN$_x$ and Ni$_1$@mpgCN$_x$-3D. **Figure 4a** shows the X-ray absorption near edge structure (XANES) spectra of these two catalysts and of NiO, LiNiO$_2$, and Ni foil selected as reference materials for such measurements. The pre-edge features near 8333 eV are observed due to the electronic transition from 1s orbitals to 3d orbitals. The main absorption edges are observed between 8345 and 8355 eV for all the materials, resulting from the transition of a 1s electron to empty 4p orbitals. In the case of Ni$_1$@mpgCN$_x$-3D and Ni$_1$@mpgCN$_x$, characteristic features are visible between the pre-edge and main edge due to the electronic transition from 1s to 4p_z orbitals, which allowed us to hypothesize a Ni-N$_4$ structure with no bond along 4p_z orbital.[63,64] Despite XANES data for Ni$_1$@mpgCN$_x$-3D being noisy due to low nickel concentration, the spectral features display a high degree of similarity to those
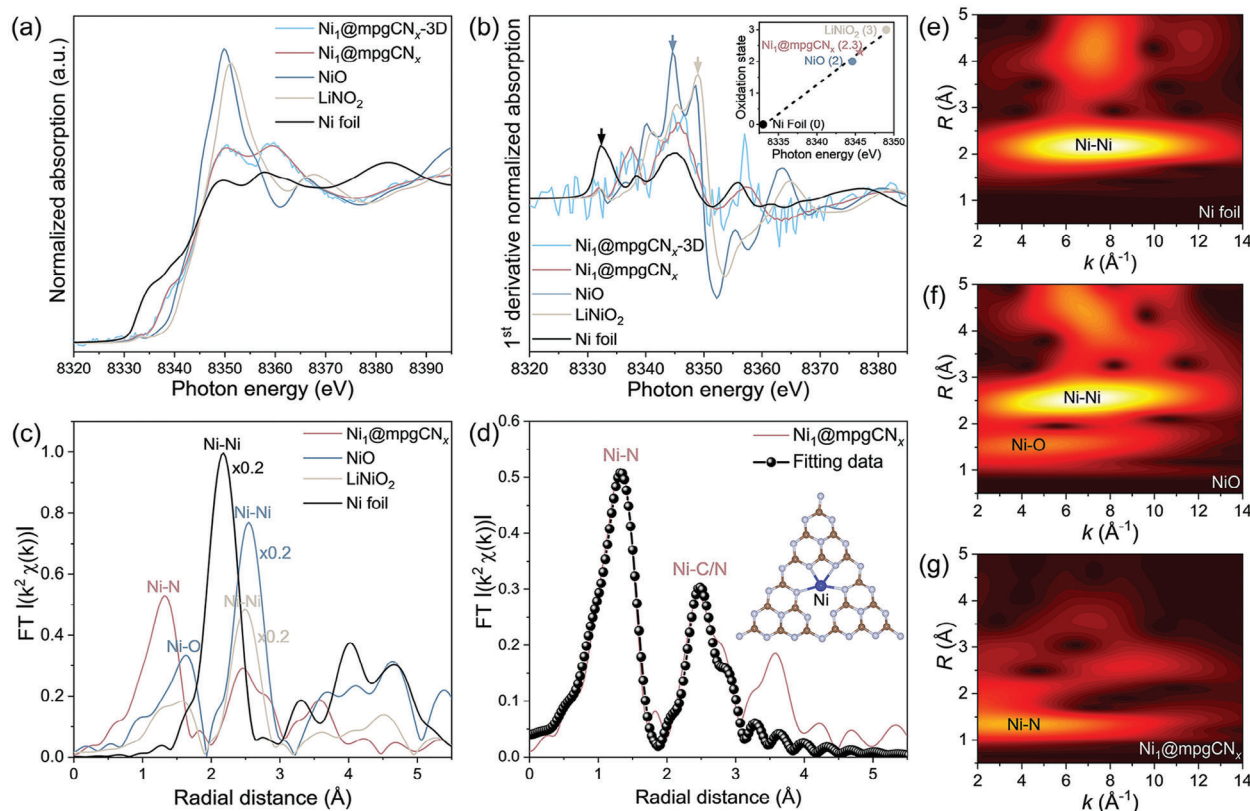
Figure 4. Normalized Ni K-edge XANES spectra a) and first derivative XANES spectra b) of $Ni_1@mpgCN_x$, $Ni_1@mpgCN_x$-3D, and nickel-containing reference materials; Fourier transform EXAFS spectra of $Ni_1@mpgCN_x$ and nickel-containing reference materials in the R-space c); EXAFS fitting curve applied to the Fourier-transform EXAFS spectra of $Ni_1@mpgCN_x$ d); WT-EXAFS analysis for Ni foil e), NiO f), and $Ni_1@mpgCN_x$ g).

of $Ni_1@mpgCN_x$. Therefore, it can be inferred that the electronic and local structures remain unaffected even after the loading of a low nickel content on $Ni_1@mpgCN_x$-3D during the 3D printing fabrication.

The oxidation state of the active nickel species in $Ni_1@mpgCN_x$ and $Ni_1@mpgCN_x$-3D was determined by comparing their first derivative XANES plot with those of the reference materials. In Figure 4b, the colored arrows indicate the maxima of these XANES graphs for the references – Ni foil, NiO, $LiNiO_2$ – in which nickel atoms have different oxidation states – 0, +2, +3, respectively. After plotting the oxidation state of each reference material against their corresponding edge incident photon energy (Figure 4b, inset), the average oxidation state of the nickel species in $Ni_1@mpgCN_x$ (2.3) was finally found as a numeric value close to previously published nickel-based SACs.[65]

Fourier transform of k^2-weighted data was used to obtain extended X-ray absorption fine structure (EXAFS) spectra (Figure 4c) to assess the local coordinative environment around the nickel species in $Ni_1@mpgCN_x$. Ni-N bonding was found to be the strongest in the EXAFS data for $Ni_1@mpgCN_x$, in contrast to NiO, $LiNiO_2$, and Ni foil where Ni-Ni bonding is the strongest. This indicates that the Ni atoms in $Ni_1@mpgCN_x$ are primarily surrounded by nitrogen atoms belonging to the support material. Such conclusion is also supported by the EXAFS fitting of the experimental data, which shows a remarkable match with

the theoretical model frequently reported for CN_x-based SACs (Figure 4d), in which the nickel active centers are coordinated by four neighboring nitrogen atoms. The results of the EXAFS fitting are summarized in Table S1 (Supporting Information).

Wavelet-transformed (WT)-EXAFS analyses were carried out to gain further insights into in the local environment of Ni foil, NiO, and $Ni_1@mpgCN_x$, by showing the wavelet of k-space and radial distribution of R-space simultaneously (Figures 4e-g). The wavelet for Ni-N bonding of $Ni_1@mpgCN_x$ and Ni-O bonding of NiO was found to be the highest at ≈ 4 Å^{-1} in k-space, and this similarity in maxima in k-space is due to the similar atomic number of nitrogen and oxygen. Therefore, the radial distribution near 1.4 Å for $Ni_1@mpgCN_x$ in R-space indicates Ni-N or Ni-O bonding instead of Ni-Ni, which in turn shows the maxima point at ≈ 7 Å^{-1} in k-space (see Figure 4e,f). From these results, it can be concluded that $Ni_1@mpgCN_x$ contains a Ni-N$_4$ architecture, as already suggested in recent works found in the literature,[66,67] preserving the monoatomic nature of the nickel species, without metal agglomeration to form clusters of nanoparticles.

Computational fluid dynamics (CFD) studies were carried out to investigate the transport phenomena occurring in reactors containing the 3D-printed structured catalysts. The velocity field inside a reactor that incorporates a 3D-printed body, whose structure resembles that of spiral-shaped twists or static mixers, was compared to that of an equivalent slurry-type tubular reactor composed of a standard open tube with suspended catalyst particles.
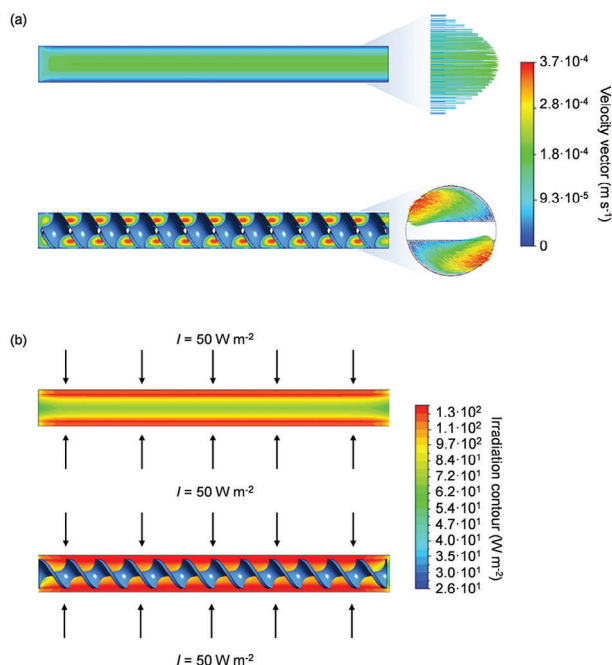
Figure 5. CFD simulations of the continuous-flow photocatalytic system. Velocity contour and velocity vectors in a reactor without a, top) and with a, bottom) a catalytic structured body; radiation field in a reactor without b, top) and with d, bottom) a catalytic structured body.

Figure 6. Turbulence kinetic energy profile in a tube reactor with and without a catalytic structured body.

Operative conditions for this set of simulations are reported in Table S2 (Supporting Information). The resulting data displayed in **Figure 5a** (top) showcase how the velocity profile obtained in the reactor with suspended particles followed the typical laminar profile. This is consistent with the obtained value of the Reynolds number, defined as in Equation 1:

$$Re = \frac{\rho_{mix} v D}{\mu_{mix}} = 0.4 \qquad (1)$$

where ρ_{mix}, μ_{mix}, v and D are the mixture density, the mixture viscosity, the spatial velocity, and the pipe diameter, respectively. This profile can have a detrimental effect in a photochemical reaction as it does not allow the recirculation of the reaction mixture in the reactors. In addition, in the context of a reactor without a structured catalyst, such as a traditional slurry-type tubular reactor, the light density was exponentially attenuated inside the domain, with major consequences on both catalytic conversion and productivity of the overall system.[68] On the other hand, the velocity profile shown in Figure 5a (bottom), related with the reactor containing a technical body with spiral-shaped twists, suggested that such configuration was capable of effectively recirculating the flow in the domain, allowing for a more homogeneous distribution of the mixture in the irradiated area within its structure. Moreover, the spiral-shaped twisted bodies are known for inducing higher levels of turbulence compared to systems without mixing elements. In a set of simulations, the maximum turbulent kinetic energy was defined as in Equation 2:

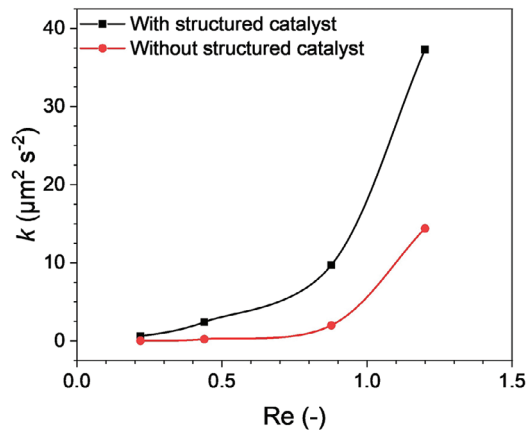$$k = \frac{1}{2}\left(\overline{(u')^2} + \overline{(v')^2} + \overline{(w')^2}\right) \qquad (2)$$

where $\overline{(u')^2}$, $\overline{(v')^2}$, $\overline{(w')^2}$ are the velocity fluctuations in the three directions of space. Table S2 (Supporting Information) and **Figure 6** show that in systems comprising of a structured catalyst, higher peak values of turbulence were reported even at very low Re values.

The radiation field was also evaluated and compared in both reactor configurations, namely without and with structured 3D-printed catalyst, using the boundary conditions previously reported. The catalyst suspension in a slurry-type tubular reactor can be considered as a pseudo-homogeneous medium,[69] and both the absorption and scattering coefficients can be assumed as independent from the position in the domain.[70] Conversely, in the second configuration, the catalyst is part of the reactor system, and for this reason, the absorption and scattering phenomena in the fluid is much lower than in conventional slurry-type reactors.[71] Figure 5b shows a graphical representation of the light distribution modelled in the reactor that includes the structured catalyst (Figure 5b, bottom) and in the slurry-type tubular reactor (Figure 5b, top). As expected, the incoming radiation in the latter decreases along the optical path, i.e., the reactor diameter. Combined with the laminar profile previously mentioned, this may lead to a non-homogeneous reaction environment concentrated in the irradiated areas of the reactor. A different result was obtained considering the setups containing a 3D-printed catalytic body as here the light can diffuse more homogeneously in the domain up to the structured catalyst itself. Moreover, the recirculation induced by the spiral-shaped architecture of the catalytic body ensures a more homogeneous exposure of the reaction mixture to the catalysts surface. As a result of these calculations, improved performances of the reactors containing 3D-printed catalytic bodies are expected in photocatalytic experiments compared to those of traditional slurry-type reactors.

2.3. Catalytic Performance of the 3D-Printed Catalysts

The 3D-printed structured catalysts were evaluated in a relevant continuous-flow photocatalytic process, namely the oxidation of benzyl alcohol to benzaldehyde, in order to assess their potential application in an industrial scenario. The choice of this model reaction was motivated by its relevance for the conversion of

biomass-derived benzyl alcohol into a value-added chemical,[72] i.e., benzaldehyde, which is widely employed as a building block in the food, chemical, and pharmaceutical industries.[73] The continuous-flow photocatalytic setup comprised a syringe pump, a tubular quartz tube containing the structured body reactor in it, and blue LED lamps as irradiation source. The oxidation reaction was conducted using acetonitrile (MeCN) as solvent, at room temperature and with 2 h of residence time. After a set of control experiments reported in Table S4 (Supporting Information) that confirmed the (photo)catalytic nature of the process, the activity of mpgCN$_x$-3D and Ni$_1$@mpgCN$_x$-3D was compared with that of the resin not loaded with any powdered catalyst (Table S4, Supporting Information). The 3D-printed catalysts showed improved catalytic performance with respect to that of the bare resin, once again indicating the catalytic activity of the CN$_x$-based catalysts embedded within the 3D-printed

structures. Moreover, despite minor changes in product selectivity, the Ni$_1$@mpgCN$_x$-3D exhibited an enhanced catalytic production of benzaldehyde (20 mmol$_{prod}$ mg$_{cat}^{-1}$ h^{-1}) with respect to mpgCN$_x$-3D (17.9 mmol$_{prod}$ mg$_{cat}^{-1}$ h^{-1}). This could be explained by ligand-to-metal charge transfer phenomena occurring in CN$_x$-containing materials, which increase the photocatalytic performance of the system by facilitating electron transfer from the support to the active metal centers.[47] To understand the real advantages of this novel architecture with respect to known benchmark configurations, the catalytic performance of Ni$_1$@mpgCN$_x$-3D was compared to that of a standard packed-bed reactor loaded with Ni$_1$@mpgCN$_x$ and glass beads as inert. The outcome of these tests, shown in **Figure 7a**, highlighted the improved efficiency of the structured system (20 vs 14 mmol$_{prod}$ mg$_{cat}^{-1}$ h^{-1}), mainly related to the enhanced light diffusion and flow turbulence due to the spiral-shaped geome-
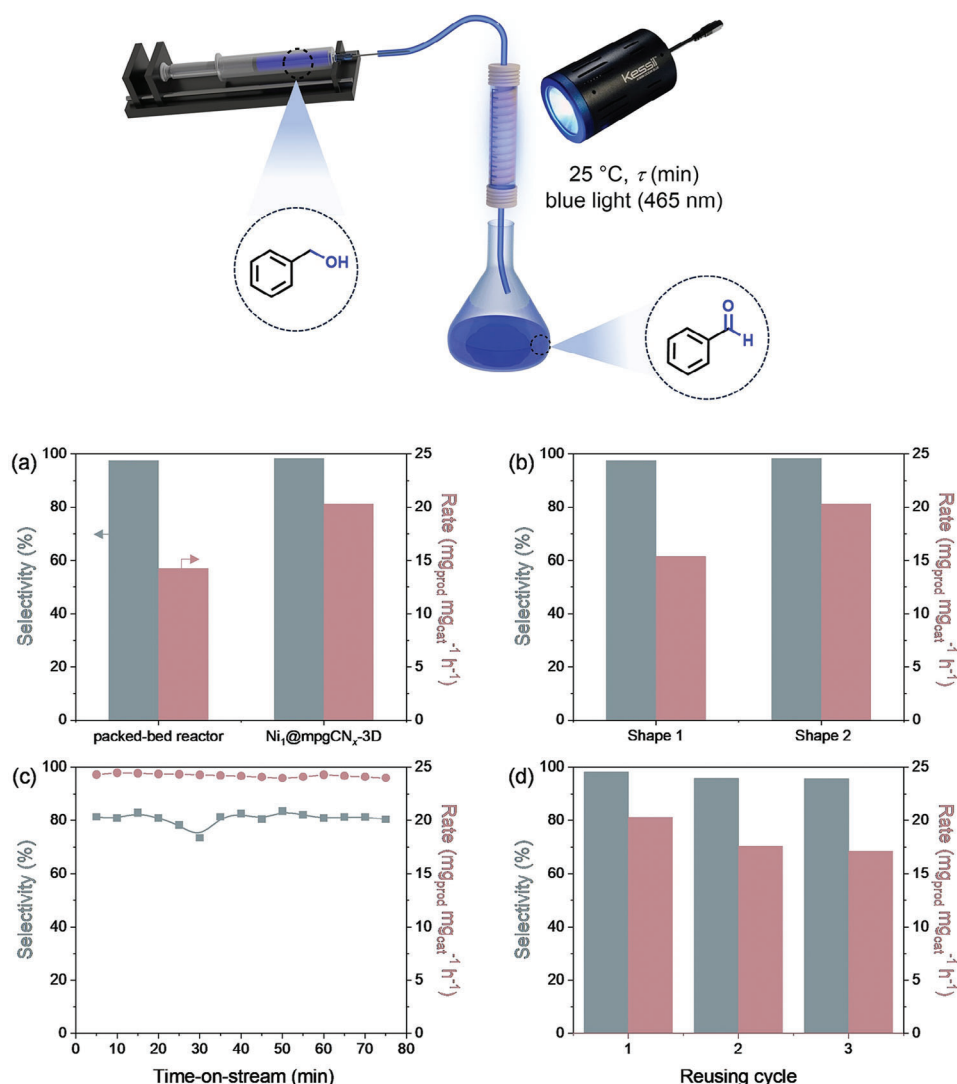

Figure 7. Benzyl alcohol oxidation employing a Ni$_1$@mpgCN$_x$ packed-bed reactor and Ni$_1$@mpgCN$_x$-3D in structured form a); effect of the shapes of the spiral twists on the reaction rate and selectivity of Ni$_1$@mpgCN$_x$-3D (shapes 1 and 2, Supporting Information) b); time-on-stream experiment with Ni$_1$@mpgCN$_x$-3D c); recycling test with Ni$_1$@mpgCN$_x$-3D d). For a), c), and d) the reactor shape considered is the 2 (See Figure S1b, Supporting Information). Reaction conditions in the Experimental Section.

**ADVANCED
SCIENCE NEWS**

www.advancedsciencenews.com

**ADVANCED
FUNCTIONAL
MATERIALS**

www.afm-journal.de

try. The effect of the architecture of the spiral-shaped twists in the 3D-printed catalysts was also investigated, as it may have an impact both on the diffusion of light across the reaction mixture and on the ability of the structured catalysts to work similarly to static mixers in flow reactors (Figure 7b). Two types of spiral twists were selected and applied for the fabrication of Ni_1@mpgCN$_x$-3D catalysts (Figure S1, Supporting Information). Shape 2 of Ni_1@mpgCN$_x$-3D correlated with an enhanced catalytic activity of the 3D-printed catalyst (Figure S1b, Supporting Information) probably due to its ability to generate an increased turbulence in the reaction solution with respect to shape 1, leading to an increased mass transfer and ultimately resulting in an improved performance.[74,75] A time-on-stream experiment was carried out along benzyl alcohol oxidation employing the Ni_1@mpgCN$_x$-3D catalyst, with aliquots of the reaction mixture regularly withdrawn during the 2 h of residence time (Figure 7c). No drops in aldehyde production were detected, demonstrating a remarkable stability of the structured catalyst in terms of activity and product selectivity. Finally, catalyst recyclability was evaluated subjecting Ni_1@mpgCN$_x$-3D to a recycling test encompassing three reaction cycles: even though a minor decrease in aldehyde production was observed, the structured catalyst retained its quantitative selectivity, proving the recyclability of the catalytic system (Figure 7d). ICP-OES analysis performed on the reacted solution revealed the absence of metal leaching from the technical body during the reaction. As additional evidence of the chemical stability and versatility of our 3D-printed SAC in diverse chemical processes, we investigated their possible dissolution in common organic solvents, as depicted in Figure S8 and Table S5 (Supporting Information). Dissolution tests employing both polar (EtOH, MeCN, DMSO, DMF, acetone) and apolar (Et$_2$O, THF, hexane, toluene) solvents highlighted an overall structural integrity of the technical bodies, validating the potential applicability of the 3D-printed structured catalysts in various chemical environments for organic transformations.

3. Conclusion

In conclusion, we have successfully harnessed photopolymerization 3D printing for the direct manufacturing of stable and active structured single-atom catalysts. Combining the inherent physicochemical and electronic properties of CN$_x$ with its ability to coordinate isolated metal species, we have directly shaped CN$_x$-based catalysts in a structured form, avoiding the exploitation of extensive and challenging washcoating procedures. This fabrication strategy was applied employing both metal-free and nickel-containing powdered catalysts mixed with a resin, and the homogeneous dispersion of the CN$_x$ catalysts in the resulting structured bodies was preserved. Furthermore, the 3D-printed catalysts exhibited remarkable performance in terms of activity and selectivity in continuous-flow photocatalytic applications, showcasing at the same time excellent recyclability and chemical stability in diverse chemical environments. This study not only unveils a novel protocol for the efficient manufacturing of 3D-printed SACs, but also opens new perspectives in the design of tailored catalysts and their application across several domains in the chemical and pharmaceutical industries.

4. Experimental Section

Synthesis of the Powdered Catalysts: The powdered Ni_1@mpgCN$_x$ catalyst was synthesized with a previously reported hard template-assisted method.[66] NiCl$_2$ (48 mg; Sigma–Aldrich, 98%) and cyanamide (3 g; Sigma–Aldrich, 99%) were added to a 40% aqueous suspension of 12 nm particles of SiO$_2$ (7.5 g; Ludox HS40, Sigma–Aldrich), and the mixture was heated at 70 °C for 16 h while kept under stirring in order to evaporate the water. The resulting white solid was then calcined in air at 550 °C for 4 h in an alumina crucible (heating ramp: 2.2 °C min^{-1}). The obtained yellow powder was briefly grounded and treated with a 4.2 M solution of NH$_4$HF$_2$ (12 g in 50 mL of water; Sigma–Aldrich, 95%), and the suspension was stirred at room temperature for 24 h and subsequently centrifuged to isolate the solid product. Upon washing with abundant water and ethanol, the product was dried under vacuum at 60 °C overnight. The powdered mpgCN$_x$ catalyst without nickel was prepared following the same procedure, but without adding the inorganic nickel salt in the first step of the synthesis protocol.

Design and Fabrication of the Structured Catalysts: mpgCN$_x$ or Ni_1@mpgCN$_x$ (0.3 g) were mixed with a commercial 3D printing resin (30 g; Anycubic, water-washed resin) to obtain a mixture with a weight catalyst:resin ratio of 1:100. The suspension was stirred at room temperature for 12 h in an amber vial, and subsequently sonicated for 1 h to further favor the homogeneous dispersion of the catalyst in the mixture. The design of the structured catalysts architecture was developed through computer-aided design (CAD) resorting to the Autodesk Inventor software: spiral column and spiral split-and-combine designs were selected and fabricated. A picture of a CAD model used for the catalysts 3D printing is depicted in Figure S1 (Supporting Information). To ensure printability and stability of the produced structures, the printing parameters were set as follows: 40 s bottom exposure time, 8 s normal layer exposure time, 50 μm layer height. The structured catalysts were 3D-printed by photopolymerization on an Elegoo Mars 2 Pro MSLA 3D printer, allowing to print 3D materials in a layer-by-layer configuration. The freshly produced structured catalysts were then washed with ethanol and subsequently dried at room temperature for 2 h. The 3D-printed catalytic architectures measured 6 mm in diameter and 60 mm in length, with a spiral torsion angle of 45°. In particular, the length and diameter were predetermined to these specific values based on the dimensions of the column hosting the structure bodies in the continuous-flow experiments.

Characterization of the Powdered and Structured Catalysts: Inductively coupled plasma optical emission spectroscopy (ICP-OES) was performed using a PerkinElmer Optima 8300 ICP-OES spectrometer to determine the nickel content in Ni_1@mpgCN$_x$ and Ni_1@mpgCN$_x$-3D. The elemental composition of all the samples was determined by combustion analysis using a Vario MICRO Elemental Analyzer, following their combustion at high temperatures (> 1000 °C) in an oxygen-rich environment. Powder X-ray diffraction (XRD) patterns were collected on a Bruker D2 Phaser diffractometer equipped with a Cu Kα radiation source (λ = 1.54 Å), and each XRD diffractogram was acquired using a 2θ step size of 0.016° and a counting time of 0.4 s per step. The chemical nature and bonding environment of the samples were assessed through Fourier-transform infrared (FTIR) spectroscopy with a Smart iTX accessory for ATR measurements mounted on a Thermo Scientific Nicolet iS20 FTIR Spectrometer equipped with a DTGS detector. 128 scans were acquired at a 4 cm^{-1} resolution, and then averaged to get the final infrared spectrum in the 4000–400 cm^{-1} wavenumber range. Nitrogen physisorption measurements were carried out on a Micromeritics ASAP 2020 instrument at −196 °C, and before the measurement, the samples were degassed at 150 °C for 24 h. The specific surface area was determined by the Brunauer-Emmett-Teller (BET) method using the adsorption branch in the p/p_0 range from 0.05 to 0.30. Thermal gravimetric analysis (TGA) was carried out with a PerkinElmer STA 6000 analyzer. For each analysis, samples were heated from 30 to 900 °C at a heating rate of 10 °C min^{-1}. The cross-polarization/magic angle spinning (CP/MAS) ^{13}C NMR spectra were recorded on a Bruker FT-NMR Avance TM 500 with a superconducting ultra shield magnet of 11.7 Tesla operating at 125.76 MHz ^{13}C frequency. The following

conditions were applied: repetition time 4 s, contact time 8 ms, and spin rate 10 kHz. The compounds were finely ground and placed in zirconium rotors (4 mm in diameter and 18 mm in height) before being introduced in the instrument. Transmission electron microscopy (TEM) micrographs were collected using a double Cs-corrected JEOL JEM-ARM200F (S)TEM operated at 80 kV and equipped with a cold field emission gun. Energy dispersive X-ray spectroscopy (EDS) analyses were performed employing a JEOL silicon drift detector (DrySD60GV; sensor size, 60 mm^2) with a solid angle of $\approx$0.6 srad. HAADF-STEM imaging was carried out using a Nion UltraSTEM100 microscope equipped with a cold field emission electron source and a quadrupole-octupole aberration corrector in the probe-forming electron optics, operated at 60 keV. Confocal laser scanning microscopy (CLSM) measurements were performed on a custom-built confocal setup. Additional information on equipment and protocols related to CLSM and fluorescence-lifetime imaging microscopy (FLIM) are included in the Supporting Information. Nano computed tomography scanning was conducted using an industrial micro-CT system (BIR Actis 130/150, upgraded). Scanning plane was horizontal and perpendicular to the axis of the sample. Based on geometry and dimensions of the sample, a spheric voxel of 8 × 8 × 8 µm was obtained. Segmentation of 2D slices obtained from the micro-CT technique was carried out by means of AvizoMercury software. Ex situ X-ray absorption spectroscopy (XAS) measurements were carried out at the 10C Wide XAFS beamline (BL10C) of the Pohang Light Source-II (PLS-II). The incident monochromatic X-ray beam was shaped using a Si(111) double crystal monochromator which rejected harmonic by detuning the beamline optics, thereby reducing the intensity of the incident beam by 40%. The slits used in all the measurements had an opening of 1 mm (vertical) × 5 mm (horizontal). The measurements were conducted at the Ni K-edge, in transmission mode, and the detectors used were based on ionization chambers.

Photocatalytic Continuous-Flow Setup and Experiments: The photocatalytic continuous-flow reactions were conducted with an experimental setup that included a blue LED lamp (Kessil H150 Blue), a syringe pump (Harvard PHD ULTRA CP), and a column reactor (Diba Omnifit column, 6 mm i.d, 150 mm length). The LED lamp was placed 5 cm away from the reactor, which contained the 3D-printed structured catalyst. A picture of the setup is reported in Figure S2 (Supporting Information). In a typical experiment, a 0.04 M solution of benzyl alcohol (60 mg, 0.55 mmol, Sigma–Aldrich, 99%) in acetonitrile (MeCN, 15 mL, Sigma–Aldrich, 99%) was introduced by the syringe pump, operating at *quasi*-ambient pressure, into the assembled reactor at room temperature (flow rate = 3 mL h^{-1}). For sake of comparison, a photocatalytic test with packed bed reactor composed by the same column reactor filled with Ni$_1$@mpgCN$_x$ (10 mg) and glass beads (1 g) was conducted. Before initiating the irradiation of the reactor setup, a control experiment was carried out by collecting and analyzing separately 2 mL of the reaction mixture. Subsequently, the LED lamp was activated, and the resulting solution was collected and analyzed through high-performance liquid chromatography (HPLC). 30 µL of the reaction mixture were diluted with 130 µL of MeCN and injected in an Agilent 1200 chromatograph equipped with a UV detector G1315D working at $\lambda =$ 210 nm, and a C18 HypersilGOLD 5 µm 175 Å column (Thermo-Fisher). Samples were analyzed using MeCN/H$_2$O 60:40 as a mobile phase, with a total flow rate of 0.7 mL min^{-1} at 40 °C. Reaction rate and selectivity were calculated using the calibration curves related to the starting material (benzyl alcohol) and product (benzaldehyde).

Computational Fluid Dynamics Simulations: The first photochemical reactor model used for the computational fluid dynamics (CFD) simulations is equipped with a 3D-printed structured body whose architecture resembles that of spiral-shaped twists or static mixers (Figure S3a, Supporting Information), while the second reactor is composed of a standard open tube with suspended catalyst particles (Figure S3b, Supporting Information). Notably, for the former, the same 3D printing STL file used during additive manufacturing was employed to reconstruct the technical body in the CFD simulation programme. Both the reactor model structures have a length of $L = 62$ mm and a diameter equal to $D = 5$ mm. The continuity, momentum, and species mass transport were solved using the Ansys Fluent suite of programs through a Reynolds-Averaged-Navier-Stokes (RANS) approach. The Shear-Stress Transport (SST) k-ω model was cho-

sen due to its capability of correctly reproducing the flow within a wide range of fluid dynamic regimes.[76,77] In order to have reliable results independent from the grid, a mesh independence analysis was conducted. For this reason, a series of simulations were performed considering the reactor containing the spiral-shaped structured body and meshes composed of increasing number of cells, and the pressure drop was monitored at the outlet of the reactor. The operative conditions for this set of simulations are reported in Table S2 (Supporting Information). From the results shown in Figure S4 (Supporting Information), no significant variations above 1.8·10^6 cells can be observed, thus demonstrating that independence from the grid is reached. The same cell dimensions were kept for the empty tubular reactor. To model the radiation field inside the reactor, the Radiative Transfer Equation (RTE, Equation 3) was solved:

$$\frac{dI\left(\vec{r}, \vec{s}\right)}{dt} + (k + \sigma_s)\, I\,(\vec{r}, \vec{s}) = an^2 \frac{\sigma T^4}{\pi} + \frac{\sigma_s}{\pi} \int_0^{4\pi} I(\vec{r}, \vec{s})\Phi\left(\vec{s} \cdot \vec{s}'\right) \tag{3}$$

where $\vec{r}$ and $\vec{s}$ are the position vectors, $\vec{s}'$ is the scattering direction vector, s is the path length, n is the refractive index, σ_s is the scattering coefficient, k is the absorption coefficient, σ is the Stefan-Boltzmann constant, I is the radiation intensity (which depends on position vectors), Φ is the phase function, and Ω' is the solid phase angle. The Discrete Ordinate Model (DOM) was selected to solve the RTE thanks to its ability to provide an accurate solution to this equation:[77,78] the domain was subdivided into a finite number of discrete solid angles, each associated with a vector direction fixed within the Cartesian system ($\vec{x}, \vec{y}, \vec{z}$).[77] The utilization of a sufficiently high angular discretization and pixelization was required to avoid the "ray effect" and angle overhang, respectively. In our previous work,[78] it was found that an angular discretization of 8 and a pixelization of 3 was enough to ensure reliable results, and for this reason, these values were adopted also in this work. To model the radiation field inside the reactor equipped with a 3D-printed structured body and inside the empty tubular reactor, an external domain was added to the geometry (as shown in Figure S3, Supporting Information). Two walls were set as semi-transparent, with an incoming radiation I equal to $I = 50$ W m^{-2}. The other walls of the external domain were set as semi-transparent, and the 3D-printed body was set as opaque, with an emissivity equal to 1. Assuming that the tubular reactor in Figure S3b (Supporting Information) was loaded with a slurry of catalyst having the same catalyst concentration as the 3D-printed body (roughly $C_{cat} = 0.01$ g cm^{-3}), the absorption and scattering coefficients can be expressed by Equations 4 and 5:[69]

$$k = k^* \cdot C_{cat} \left[\frac{1}{m}\right] \tag{4}$$

$$\sigma_s = \sigma_s^* \cdot C_{cat} \left[\frac{1}{m}\right] \tag{5}$$

where k^* and σ_s^* are the specific absorption and scattering coefficients calculated for a similar catalyst commonly used in photochemical reactions, respectively. Since the technical body contains the catalyst in it,[71] it was assumed that the reaction mixture has negligible absorption and scattering coefficient values compared to the catalyst itself. The absorption coefficient of the catalytic layer is not known, so it was assumed to be the same calculated for the slurry reactor. A series of simulations to ensure independent results was performed considering different values of the specific absorption coefficient: in particular, k values equal to 50, 80, and 100 m^{-1} were considered. The volume-averaged incident radiation on the fluid was 91, 90, and 90 W m^{-2}, confirming that for the considered conditions the influence of the mixing elements absorption on the radiation field of the fluid had negligible influence.

Supporting Information

Supporting Information is available from the Wiley Online Library or from the author.

Acknowledgements

Conflict of Interest

The authors declare no conflict of interest.

Data Availability Statement

The data that support the findings of this study are available from the corresponding author upon reasonable request.

Keywords

[1] E. Roduner, *Chem. Soc. Rev.* **2014**, *43*, 8226.

[2] X. Cui, W. Li, P. Ryabchuk, K. Junge, M. Beller, *Nat. Catal.* **2018**, *1*, 385.

[3] F. Zaera, *Chem. Rev.* **2022**, *122*, 8594.

[4] C. M. Friend, B. Xu, *Acc. Chem. Res.* **2017**, *50*, 517.

[5] G. Vilé, D. Albani, M. Nachtegaal, Z. Chen, D. Dontsova, M. Antonietti, N. López, J. Pérez-Ramírez, *Angew. Chem., Int. Ed.* **2015**, *54*, 11265.

[6] A. Wang, J. Li, T. Zhang, *Nat. Rev. Chem.* **2018**, *2*, 65.

[7] H. Liu, Q. Lei, R. Miao, M. Sun, C. Qin, L. Zhang, G. Ye, Y. Yao, B. Huang, Z. Ma, *Adv. Funct. Mater.* **2022**, *32*, 43.

[8] H. Li, M. Wang, L. Luo, J. Zeng, *Adv. Sci.* **2019**, *6*, 1801471.

[9] D. Liu, J. Li, S. Ding, Z. Lyu, S. Feng, H. Tian, C. Huyan, M. Xu, T. Li, D. Du, P. Liu, M. Shao, Y. Lin, *Small Methods* **2020**, *4*, 1900827.

[10] G. Meng, J. Sun, L. Tao, K. Ji, P. Wang, Y. Wang, X. Sun, T. Cui, S. Du, J. Chen, D. Wang, Y. Li, *ACS Catal.* **2021**, *11*, 1886.

[11] V. B. Saptal, V. Ruta, M. A. Bajada, G. Vilé, *Angew. Chem., Int. Ed.* **2023**, *62*, 202219.

[12] Y. Zhang, J. Zhao, H. Wang, B. Xiao, W. Zhang, X. Zhao, T. Lv, M. Thangamuthu, J. Zhang, Y. Guo, J. Ma, L. Lin, J. Tang, R. Huang, Q. Liu, *Nat. Commun.* **2022**, *13*, 58.

[13] J. Sui, H. Liu, S. Hu, K. Sun, G. Wan, H. Zhou, X. Zheng, H. Jiang, *Adv. Mater.* **2022**, *34*, 2109203.

[14] L. Shi, X. Ren, Q. Wang, Y. Li, F. Ichihara, H. Zhang, Y. Izumi, L. Ren, W. Zhou, Y. Yang, J. Ye, *Small* **2020**, *16*, 2002356.

[15] G. Gentile, M. Marchi, M. Melchionna, P. Fornasiero, M. Prato, G. Filippini, *European J. Org. Chem.* **2022**, *37*, 202200944.

[16] L. A. Cipriano, G. Di Liberto, G. Pacchioni, *ACS Catal.* **2022**, *12*, 11682.

[17] L. Suhadolnik, M. Bele, M. Čekada, P. Jovanovič, A. Maselj, A. Lončar, G. Dražić, M. Šala, N. Hodnik, J. Kovač, T. Montini, M. Melchionna, P. Fornasiero, *Chem. Mater.* **2023**, *35*, 2612.

[18] R. Langer, E. Fako, P. Błoński, M. Vavrečka, A. Bakandritsos, M. Otyepka, N. López, *Appl. Mater. Today* **2020**, *18*, 100462.

[19] L. Yu, Y. Li, Y. Ruan, *Angew. Chem., Int. Ed.* **2021**, *60*, 25296.

[20] H. Wei, K. Huang, D. Wang, R. Zhang, B. Ge, J. Ma, B. Wen, S. Zhang, Q. Li, M. Lei, C. Zhang, J. Irawan, L.-M. Liu, H. Wu, *Nat. Commun.* **2017**, *8*, 1490.

[21] X. Chen, S. Guan, J. Zhou, H. Shang, J. Zhang, F. Lv, H. Yu, H. Li, Z. Bian, *Angew. Chem., Int. Ed.* **2023**, *62*, 202312734.

[22] Z. Song, Q. Wang, J. Li, K. Adair, R. Li, L. Zhang, M. Gu, X. Sun, *EcoMat* **2023**, *5*, e12351.

[23] X. Li, A. Surkus, J. Rabeah, M. Anwar, S. Dastigir, H. Junge, A. Brückner, M. Beller, *Angew. Chem., Int. Ed.* **2020**, *59*, 15849.

[24] S. Mitchell, N.-L. Michels, J. Pérez-Ramírez, *Chem. Soc. Rev.* **2013**, *42*, 6094.

[25] H. Zhang, T. Tang, H. Wang, H. Wang, Y. Cao, H. Yu, *Adv. Funct. Mater.* **2024**, 2312939.

[26] C. Y. Chaparro-Garnica, P. Jordá-Faus, E. Bailón-García, R. Ocampo-Pérez, C. G. Aguilar-Madera, A. Davó-Quiñonero, D. Lozano-Castelló, A. Bueno-López, *ACS Appl. Mater. Interfaces* **2020**, *12*, 54573.

[27] X. Fang, X. Wang, H. Zhang, Z. Li, J. Li, Y. Zhou, *Adv. Eng. Mater.* **2015**, *17*, 1344.

[28] Y. Yang, H. Zhang, Z. Wang, X. Li, A. Abdelsamie Abdelrahim Abdelsamie, X. Yuan, X. Fan, R. Zhang, H. Chang, *ChemElectroChem* **2020**, *7*, 2485.

[29] H. Liu, C. Li, X. Ren, K. Liu, J. Yang, *Sci. Rep.* **2017**, *7*, 16589.

[30] F. Rashidi, T. Sasaki, A. M. Rashidi, A. Nemati Kharat, K. J. Jozani, *J. Catal.* **2013**, *299*, 321.

[31] X. Zhao, Y. Xia, G. M. Whitesides, *Adv. Mater.* **1996**, *8*, 837.

[32] Y. Chen, Z. Yu, Y. Ye, Y. Zhang, G. Li, F. Jiang, *ACS Nano* **2021**, *15*, 1869.

[33] C. Parra-Cabrera, C. Achille, S. Kuhn, R. Ameloot, *Chem. Soc. Rev.* **2018**, *47*, 209.

[34] G. Vilé, D. Ng, Z. Xie, I. Martinez-Botella, J. Tsanaktsidis, C. H. Hornung, *ChemCatChem* **2022**, *14*, 202101941.

[35] A. M. Díez, F. C. Moreira, B. A. Marinho, J. C. A. Espíndola, L. O. Paulista, M. A. Sanromán, M. Pazos, R. A. R. Boaventura, V. J. P. Vilar, *Chem. Eng. J.* **2018**, *343*, 597.

[36] C.-Y. Lee, A. C. Taylor, A. Nattestad, S. Beirne, G. G. Wallace, *Joule* **2019**, *3*, 1835.

[37] Y. Gao, J. Lalevée, A. Simon-Masseron, *Adv. Mater. Technol.* **2023**, *8*, 2300377.

[38] Y. Zhao, H. Mei, P. Chang, C. Chen, L. Cheng, K. G. Dassios, *ACS Nano* **2021**, *15*, 240.

[39] A. S. Díaz-Marta, C. Yáñez, E. Lasorsa, P. Pacheco, C. R. Tubío, J. Rivas, Y. Piñeiro, M. A. G. Gómez, M. Amorín, F. Guitián, A. Coelho, *ChemCatChem* **2020**, *12*, 1762.

[40] B. J. Lee, K. Hsiao, G. Lipkowitz, T. Samuelsen, L. Tate, J. M. DeSimone, *Addit. Manuf.* **2022**, *55*, 102800.

[41] A. Hansen, M. Renner, A. G. Griesbeck, T. Büsgen, *Chem. Commun.* **2020**, *56*, 15161.

[42] T. R. Yeazel-Klein, A. G. Davis, M. L. Becker, *Adv. Mater. Technol.* **2023**, *8*, 2201904.

[43] M. Layani, X. Wang, S. Magdassi, *Adv. Mater.* **2018**, *30*, 1706344.

[44] I. Cooperstein, E. Sachyani-Keneth, E. Shukrun-Farrell, T. Rosental, X. Wang, A. Kamyshny, S. Magdassi, *Adv. Mater. Interfaces* **2018**, *5*, 1800996.

[45] D. Gräfe, A. Wickberg, M. M. Zieger, M. Wegener, E. Blasco, C. Barner-Kowollik, *Nat. Commun.* **2018**, *9*, 2788.

[46] V. Ruta, A. Sivo, L. Bonetti, M. A. Bajada, G. Vilé, *ACS Appl. Nano Mater.* **2022**, *5*, 14520.

[47] J. Liu, Y. Zou, D. Cruz, A. Savateev, M. Antonietti, G. Vilé, *ACS Appl. Mater. Interfaces* **2021**, *13*, 25858.

[48] C. M. Ho, M. C. Wu, S. H. Chen, Y. H. Chang, T. H. Lin, M. H. Jao, S. H. Chan, W. F. Su, K. M. Lee, *Sol. RRL* **2021**, *5*, 2100257.

[49] Z. Ding, X. Chen, M. Antonietti, X. Wang, *ChemSusChem* **2011**, *4*, 274.

[50] M. A. Bajada, G. Di Liberto, S. Tosoni, V. Ruta, L. Mino, N. Allasia, A. Sivo, G. Pacchioni, G. Vilé, *Nat. Synth.* **2023**, *2*, 1092.

[51] Y. Hu, Y. Shim, J. Oh, S. Park, S. Park, Y. Ishii, *Chem. Mater.* **2017**, *29*, 5080.

[52] F. Xie, X. Cui, X. Zhi, D. Yao, B. Johannessen, T. Lin, J. Tang, T. B. F. Woodfield, L. Gu, S.-Z. Qiao, *Nat. Synth.* **2023**, *2*, 129.

[53] C. Fukuhara, S. Ratchahat, A. Kamiyama, M. Sudoh, R. Watanabe, *Chem. Lett.* **2019**, *48*, 441.

[54] J. C. Kurnia, A. P. Sasmito, E. Birgersson, T. Shamim, A. S. Mujumdar, *Chem. Eng. Process. Process Intensif.* **2014**, *82*, 101.

[55] B. Dai, Y. Zhou, X. Xiao, Y. Chen, J. Guo, C. Gao, Y. Xie, J. Chen, *Adv. Sci.* **2022**, *9*, 2203057.

[56] J. S. Manzano, H. Wang, L. Qi, I. I. Slowing, *Appl. Catal. A* **2020**, *605*, 117794.

[57] J. S. Manzano, Z. B. Weinstein, A. D. Sadow, I. I. Slowing, *ACS Catal.* **2017**, *7*, 7567.

[58] G. Vilé, P. Sharma, M. Nachtegaal, F. Tollini, D. Moscatelli, A. Sroka-Bartnicka, O. Tomanec, M. Petr, J. Filip, I. S. Pieta, R. Zbořil, M. B. Gawande, *Sol. RRL* **2021**, *5*, 2100176.

[59] T. Wang, R. A. Riggleman, D. Lee, K. J. Stebe, *Mater. Horiz.* **2023**, *10*, 1385.

[60] L. Deng, L. Albertazzi, A. R. A. Palmans, *Biomacromolecules* **2022**, *23*, 326.

[61] M. A. Khan, A. J. Sprockel, K. A. Macmillan, M. T. Alting, S. P. Kharal, S. Boakye-Ansah, M. F. Haase, *Adv. Mater.* **2022**, *34*, 2109547.

[62] J. A. Levitt, P.-H. Chung, K. Suhling, *J. Biomed. Opt.* **2015**, *20*, 096002.

[63] Z. Zeng, L. Y. Gan, H. Bin Yang, X. Su, J. Gao, W. Liu, H. Matsumoto, J. Gong, J. Zhang, W. Cai, Z. Zhang, Y. Yan, B. Liu, P. Chen, *Nat. Commun.* **2021**, *12*, 4088.

[64] H. Bin Yang, S.-F. Hung, S. Liu, K. Yuan, S. Miao, L. Zhang, X. Huang, H.-Y. Wang, W. Cai, R. Chen, J. Gao, X. Yang, W. Chen, Y. Huang, H. M. Chen, C. M. Li, T. Zhang, B. Liu, *Nat. Energy* **2018**, *3*, 140.

[65] W. Wan, Y. Zhao, S. Wei, C. A. Triana, J. Li, A. Arcifa, C. S. Allen, R. Cao, G. R. Patzke, *Nat. Commun.* **2021**, *12*, 5589.

[66] G. Vilé, G. Di Liberto, S. Tosoni, A. Sivo, V. Ruta, M. Nachtegaal, A. H. Clark, S. Agnoli, Y. Zou, A. Savateev, M. Antonietti, G. Pacchioni, *ACS Catal.* **2022**, *12*, 2947.

[67] X. Liu, H. Wang, W. Li, J. Chen, J. Fang, X. Yan, S. Mi, S. Hong, M. Lei, X. Yin, L. Bai, Y. Guo, R. Xu, Z. Cheng, L. Wang, *ACS Appl. Energy Mater.* **2022**, *5*, 12991.

[68] K. Loubière, M. Oelgemöller, T. Aillet, O. Dechy-Cabaret, L. Prat, *Chem. Eng. Process. Process Intensif.* **2016**, *104*, 120.

[69] I. Grčić, G. L. Puma, *Appl. Catal. B* **2017**, *211*, 222.

[70] C. Casado, J. Marugán, R. Timmers, M. Muñoz, R. van Grieken, *Chem. Eng. J.* **2017**, *310*, 368.

[71] Y. Boyjoo, M. Ang, V. Pareek, *Chem. Eng. Sci.* **2013**, *101*, 764.

[72] Y. Zhang, G. Zhao, Y. Zhang, X. Huang, *Green Chem.* **2014**, *16*, 3860.

[73] H. Li, Y. Meng, C. Shu, X. Li, A. A. Kiss, X. Gao, *ACS Sustainable Chem. Eng.* **2018**, *6*, 14114.

[74] M. B. Plutschack, B. Pieber, K. Gilmore, P. H. Seeberger, *Chem. Rev.* **2017**, *117*, 11796.

[75] D. Koufou, S. Kuhn, *ACS Eng. Au* **2023**.

[76] J. Albertazzi, F. Florit, V. Busini, R. Rota, *Ind. Eng. Chem. Res.* **2021**, *60*, 16490.

[77] ANSYS Inc., ANSYS Fluent Theory Guide – release 19.*1*, **2018**.

[78] J. Albertazzi, F. Florit, V. Busini, R. Rota, *Chem. Eng. Process. Process Intensif.* **2022**, *182*, 109201.